Interdiffusion-Enhanced Cation Exchange for HgSe and HgCdSe Nanocrystals with Infrared Bandgaps

Wonseok Lee[1,2] and Andrew M. Smith[1,2,3,4,5,6]*

[1] Department of Bioengineering, University of Illinois Urbana-Champaign, Urbana, Illinois 61801, USA

[2] Micro and Nanotechnology Laboratory, University of Illinois Urbana-Champaign, Urbana, Illinois 61801, USA

[3] Carl R. Woese Institute for Genomic Biology, University of Illinois Urbana-Champaign, Urbana, IL 61801, USA

[4] Department of Department of Materials Science & Engineering, University of Illinois Urbana-Champaign, Urbana, Illinois 61801, USA

[5] Cancer Center at Illinois, University of Illinois Urbana-Champaign, Urbana, Illinois 61801, USA

[6] Carle Illinois College of Medicine, Urbana, IL 61801, USA

* To whom correspondence should be addressed: smi@illinois.edu

https://doi.org/10.26434/chemrxiv-2024-jx761 **ORCID:** https://orcid.org/0000-0002-0238-4816 Content not peer-reviewed by ChemRxiv. **License:** CC BY-NC-ND 4.0

ABSTRACT

Colloidal semiconductor nanocrystals based on CdSe have been precisely optimized for photonic applications in the visible spectrum, with modern products exhibiting structural uniformity, near 100% quantum yield, and linewidths narrower than 100 meV. Here we report homogeneous nanocrystals with tunable bandgaps in the infrared based on HgSe and $Hg_xCd_{1-x}Se$ alloys deriving from CdSe precursors. We find that Ag^+ catalyzes cation interdiffusion to reduce the CdSe-HgSe alloying temperature from 250 °C to 80 °C. Together with ligands that modulate surface cation exchange rates, interdiffusion-enhanced Hg^{2+} exchange of diverse CdSe nanocrystals proceeds homogeneously and completely. The products retain sizes, shapes, and uniformity of the parent nanocrystals but exhibit enhanced absorption. After passivation with heteroepitaxial CdZnS shells, photoluminescence wavelength is tunable in the shortwave infrared by composition without changing size, with 80–91% quantum yield and linewidths near 100 meV. These materials may find applications in infrared photonic devices and infrared bioimaging.

https://doi.org/10.26434/chemrxiv-2024-jx761 **ORCID:** https://orcid.org/0000-0002-0238-4816 Content not peer-reviewed by ChemRxiv. **License:** CC BY-NC-ND 4.0

INTRODUCTION

Colloidal semiconductor nanocrystals (NCs) are solution-dispersed, solution-processed nanomaterials that provide a unique combination of photophysical properties for applications in photonic devices and bioimaging. With these materials, electronic energy levels and optical bandgaps are tunable by both size and composition with large absorbance cross sections, high photoluminescence (PL) quantum yield (QY), and long-term photochemical and photophysical stability.[1] Following the first syntheses of monodispersed and size-tunable cadmium chalcogenide NCs in 1993,[2] considerable developments have been made toward NCs with controllable shapes, crystal structures, compositional heterostructures, and surface facets.[3] This structural control together with predictive models of quantized energy levels now allows the precise design of electronic transitions, dynamics, and charge interactions.[4] Visible spectrum NCs, especially prototypical CdSe NCs and their core/shell CdSe/CdZnS heterostructures, now are widely used light-emitters with PL QY near 100%, bandwidths near 100 meV, and size distributions near 5%.[5,6]

NCs with optical bandgap energies in the infrared spectrum are being pursued for applications in infrared photonic devices and deep-tissue bioimaging.[7,8] The most developed binary NC materials with infrared bandgaps include InAs, PbS, PbSe, HgSe, and HgTe, all of which are less advanced compared with their counterparts in the visible spectrum due to distinct challenges in synthesis. III-V InAs NCs are challenging to prepare with homogeneous sizes, especially for larger sizes with narrower bandgaps, while PL QY is limited by interfacial defects at heterovalent interfaces incorporating insulating II-VI shell compounds like CdSe, CdS, and ZnS.[9,10] IV-VI PbS and PbSe NCs can be synthesized with tunable bandgaps across a wide range of sizes with high monodispersity,[11,12] but shell deposition required to prevent oxidation[13,14] broadens linewidths due to lattice mismatch with II-VI shell materials and heterogeneity of shell thickness. In contrast, II-VI HgSe and HgTe NCs have homovalence and equivalent cubic zinc-blende crystal structures as canonical II-VI CdS and ZnS shells which should enable homogeneous and low-defect core/shell heterostructures with high PL QY and flexible optical tunability through the HgSe or HgTe core size.[15,16] Nevertheless, telluride-based NCs have a propensity to oxidize even with

https://doi.org/10.26434/chemrxiv-2024-jx761 **ORCID:** https://orcid.org/0000-0002-0238-4816 Content not peer-reviewed by ChemRxiv. **License:** CC BY-NC-ND 4.0

shells, and synthetic challenges remain for *de novo* synthesis of HgSe NCs. *De novo* syntheses and processing of mercury chalcogenide NCs require low temperatures (typically 0–120 °C) to avoid NC degradation and reduction of Hg^{2+} precursors (**Table S1**). This contrasts with other II-VI materials that are stable at high temperatures (typically 200–380 °C) and compatible with coordinating ligands with diverse hard and soft basic groups such as carboxylates, amines, and phosphonates. As a result, current HgSe NCs have wide size distributions (near 10–20%[17-19]) and their maturity in terms of size, shape, and heterostructure engineering lags well behind visible semiconductor NCs based on CdSe.

HgSe is further useful for its capacity to alloy with CdSe to form ternary $Hg_xCd_{1-x}Se$ alloys with wide, continuous tunability of photophysical properties, including bandgaps spanning 1.74 eV (CdSe) to –0.06 eV (HgSe), comprising the entire infrared spectrum.[15] Moreover, the lattice mismatch between CdSe and HgSe is smaller than 0.5% (a_{CdSe} = 6.05 Å, a_{HgSe} = 6.08 Å) such that there is only a small dependence of materials properties on composition.[15] These properties mirror those of $Hg_xCd_{1-x}Te$ which is the workhorse photonic material for high-performance infrared photodetectors as thin films and bulk materials due to strong infrared absorption.[20] Alloys further allow tunability of photophysical and electronic properties through composition, independently of NC size, a key design characteristic for modern applications in multispectral bioimaging.[21] However, while composition-tunable ternary II-VI NCs can be readily prepared with diverse compositions (*e.g.*, $Cd_xZn_{1-x}Se$, $CdSe_xS_{1-x}$, and $CdSe_xTe_{1-x}$), homogeneous $Hg_xCd_{1-x}Se$ NCs cannot be prepared *de novo* due to disparate reaction temperatures required for mercury and cadmium precursors.

Cation exchange (CE) reactions allow the creation of ionic NCs that cannot be readily synthesized *de novo* by exchanging “host” cations with “guest” cations, with the products inheriting the structural framework and distribution of the parent NCs. Through CE, guest compositional domains form within the parent NC through different pathways depending on the crystal structures and lattice parameters of the parent and product NC.[22] When crystal structures are equivalent, CE reactions typically proceed through a core/shell intermediate with a shell rich in guest cations, as the surface exchange rate is much faster than the rate of interdiffusion between cations within the NC.[23-25] This is the case for the reaction between

https://doi.org/10.26434/chemrxiv-2024-jx761 **ORCID:** https://orcid.org/0000-0002-0238-4816 Content not peer-reviewed by ChemRxiv. **License:** CC BY-NC-ND 4.0

CdSe NCs and Hg^{2+} cations which spontaneously displace Cd^{2+} cations to generate core/shell CdSe/HgSe NCs.[26] With the exception of very thin CdSe nanoplatelets (NPLs), these CE reactions do not approach completion to yield binary HgSe,[27] as the Hg^{2+}-Cd^{2+} interdiffusion rate is much slower in CdSe domains forming the core compared with the HgSe shell domains, effectively trapping host cations within the NC at temperatures well below the CdSe-HgSe alloying temperature (~250 °C).[28] The resulting CdSe/HgSe NCs have inferior optical properties (*vide infra*). Homogeneous alloying through ion exchange reactions is moreover rarely observed except in the case of perovskite anions.[24]

Here, we report interdiffusion-enhanced CE (IE-CE) to generate homogeneous $Hg_xCd_{1-x}Se$ alloy NCs and binary HgSe NCs (**Figure 1a**). The cation interdiffusion rate is boosted by several orders of magnitude using a monovalent silver dopant while the intrinsically rapid surface exchange rate is tuned using alkylthiol ligands. Reactions occur at low temperatures (80 °C) that yield stable colloidal products. We characterize the reaction process using chemical, physical, and optical methods to understand the reaction mechanism and compare the photophysical figures of merit relative to products of standard CE. We further grow insulating shells on the NC products toward generating high-QY and narrow-band emission at shortwave infrared (SWIR) wavelengths (photon wavelengths 1000–1700 nm or energies 1.24–0.73 eV).

https://doi.org/10.26434/chemrxiv-2024-jx761 **ORCID:** https://orcid.org/0000-0002-0238-4816 Content not peer-reviewed by ChemRxiv. **License:** CC BY-NC-ND 4.0

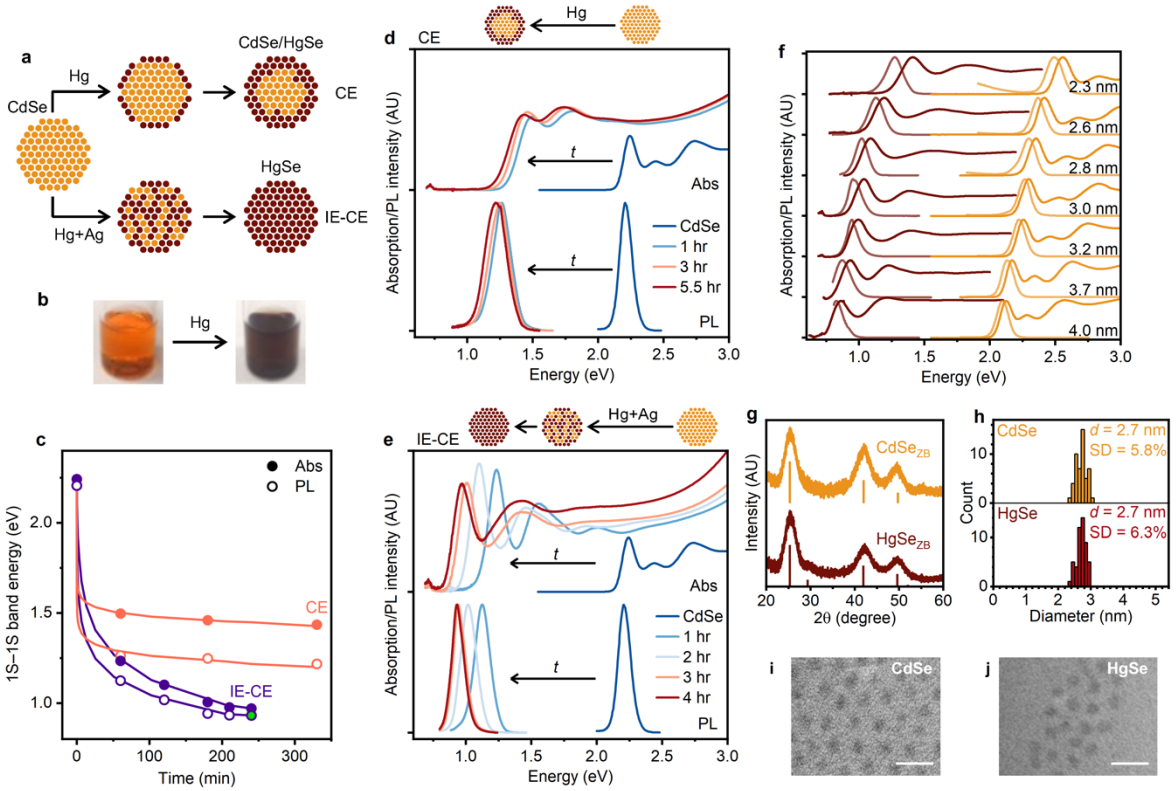

Figure 1. Interdiffusion-enhanced cation exchange (IE-CE) of CdSe nanocrystals with Hg^{2+}. (a) Schematic representation of CdSe NC exchange using either Hg^{2+} alone (CE) or in combination with Ag^{+} (IE-CE), generating either core/shell CdSe/HgSe NCs or homogeneous alloy $Hg_xCd_{1-x}Se$ NC alloys, respectively. IE-CE proceeds to yield binary HgSe NCs. **(b)** Photographs show CdSe NC solution before and 5 s after the addition of Hg^{2+} at room temperature. **(c)** Time course of spectral 1S-1S band energies for CE (orange) and IE-CE (purple), showing absorption (Abs) and photoluminescence (PL). After 4 hours of IE-CE (green-filled purple circle), the exchange of Cd^{2+} with Hg^{2+} is nearly complete (**Table S2**). **(d)** Absorption and PL spectra of 3.3 nm NCs during CE at 80 °C. Spectra are plotted in arbitrary units (AU) with absorption spectra normalized by NC concentration and PL spectra normalized by maximum intensity. **(e)** Absorption and PL spectra during IE-CE at 80 °C. Spectra are normalized as in panel (d). **(f)** Absorption and PL spectra of a size series of CdSe NCs (yellow) and their IE-CE-derived HgSe NCs (brown). PL spectra are shown in a dimmer color. All spectra are normalized by their maximum intensity values. Characterizations of 2.7 nm CdSe and HgSe NCs include **(g)** X-ray diffraction patterns with vertical lines indicating bulk zinc blende (ZB) diffraction patterns, **(h)** size histograms, and **(i,j)** transmission electron micrographs. Scale bars: 10 nm.

RESULTS

Complete cation exchange with interdiffusion enhancer. In prototypical CE and IE-CE reactions, quasi-spherical CdSe NCs with 3.3 nm diameter and zinc-blende crystal structure

https://doi.org/10.26434/chemrxiv-2024-jx761 **ORCID:** https://orcid.org/0000-0002-0238-4816 Content not peer-reviewed by ChemRxiv. **License:** CC BY-NC-ND 4.0

were dispersed in a solution containing alkylthiol and alkylamine ligands at 80 °C and treated with one of two reagents: Hg^{2+} alone or a mixture of Hg^{2+} and Ag^{+} (Hg+Ag). The color of the NC solution changed from orange-red to black immediately after the addition of either reagent (**Figure 1b**), indicating rapid replacement of a large fraction of Cd^{2+} with Hg^{2+} in the NC. The reaction proceeded to a greater extent with the Hg+Ag reagent. After 1 hour with the Hg reagent, the lowest energy absorption band (1S−1S band transition) reduced in energy by 0.74 eV (from 2.24 eV to 1.50 eV) (**Figure 1c,d**), whereas the Hg+Ag reagent induced a larger reduction of 1.00 eV (to 1.24 eV; **Figure 1c,e**), consistent with a reduction in the electronic bandgap. The emission band energy similarly decreased, with the Hg+Ag reagent yielding a shift from 2.21 eV in the middle of the visible spectrum to 1.13 eV in the SWIR. Conversion to HgSe was nearly complete in ~4 hours with the Hg+Ag reagent by elemental analysis (**Table S2**). With the Hg reagent, exchange remained incomplete even after >48 hours (**Table S3**) and could not be accelerated by further heating due to NC ripening and flocculation above 100 °C (**Figure S1**).[29,30]

A size series of CdSe NCs (2.3–4.0 nm) completely converted to HgSe NCs after several hours of reaction with the Hg+Ag reagent (**Figure 1f, Figure S2**), retaining both crystal structure (**Figure 1g**) and uniform sizes (~6% relative standard deviation of diameter; **Figure 1h-j**). Consistent with the greater degree of quantum confinement in HgSe, the HgSe NC 1S−1S transition was enhanced ~2.6-fold compared with the CdSe NCs and the dependence of spectral band energy on size was greater for HgSe across this size range (**Figure S3**). The absorbance of HgSe NCs at 400 nm wavelength (3.1 eV) was proportional to the cube of diameter as 0.0317 d^3 cm^{-1} μM^{-1} (d = NC diameter) which is larger than that of other narrow bandgap semiconductor NCs including PbS (0.0233 d^3 cm^{-1} μM^{-1})[31] and PbSe (0.0277 d^3 cm^{-1} μM^{-1})[32] (**Figure S4**) and greater than that of the parent CdSe NCs (0.0119 d^3 cm^{-1} μM^{-1} for 3.4 nm CdSe NCs). Strong absorbance at infrared wavelengths near the band edge as well as at higher energies are critical figures of merit for applications in infrared photovoltaics, photodetectors, and PL applications.[33,34]

Dependence of absorption spectra on exchange mechanism. Spectral features in **Figure 1d,e** indicate that the intermediate products of CE are core/shell CdSe/HgSe NCs

https://doi.org/10.26434/chemrxiv-2024-jx761 **ORCID:** https://orcid.org/0000-0002-0238-4816 Content not peer-reviewed by ChemRxiv. **License:** CC BY-NC-ND 4.0

while the IE-CE intermediates are homogeneously alloyed $Hg_xCd_{1-x}Se$ NCs. Absorption spectra of intermediates with equivalent PL band energies collected during the reactions are superimposed in **Figure 2a** and deconvolved into individual transitions in **Figure 2b-d**. The shapes of the absorption spectra of the CdSe NC and the IE-CE intermediate are similar, whereas there is a 67% reduction in the intensity of the 1S−1S transition in the CE intermediate. Carrier wavefunctions simulated by the effective mass approximation (EMA; **Figure 2e,f**) indicate that for both CdSe and $Hg_xCd_{1-x}Se$ NCs, electron and hole wavefunctions strongly overlap across the NC, whereas for CdSe/HgSe NCs, a pseudo-type II band alignment is formed in which electrons are localized in the shell, while holes are delocalized throughout the NC. For CdSe/HgSe NCs the electron-hole overlap decreases with increasing mercury content (x) for compositions up to x = 0.4 which explains the reduction in 1S−1S transition strength (**Figure 2g**). An increase in size from 2.3 nm to 4.0 nm enhances this charge separation, depleting up to 67% of the 1S−1S transition oscillator strength (**Figure S5**). There is also a substantial bowing of the 1S−1S band energy relative to the total composition x for CdSe/HgSe deriving from changes in the electron wavefunction shape and spatial delocalization (**Figure S6**). In contrast, for $Hg_xCd_{1-x}Se$ NCs, both calculations and empirical results show a more linear relationship between composition and both the 1S−1S transition oscillator strength (**Figure 2g**) and the 1S−1S band energy (**Figure S6**).

https://doi.org/10.26434/chemrxiv-2024-jx761 **ORCID:** https://orcid.org/0000-0002-0238-4816 Content not peer-reviewed by ChemRxiv. **License:** CC BY-NC-ND 4.0

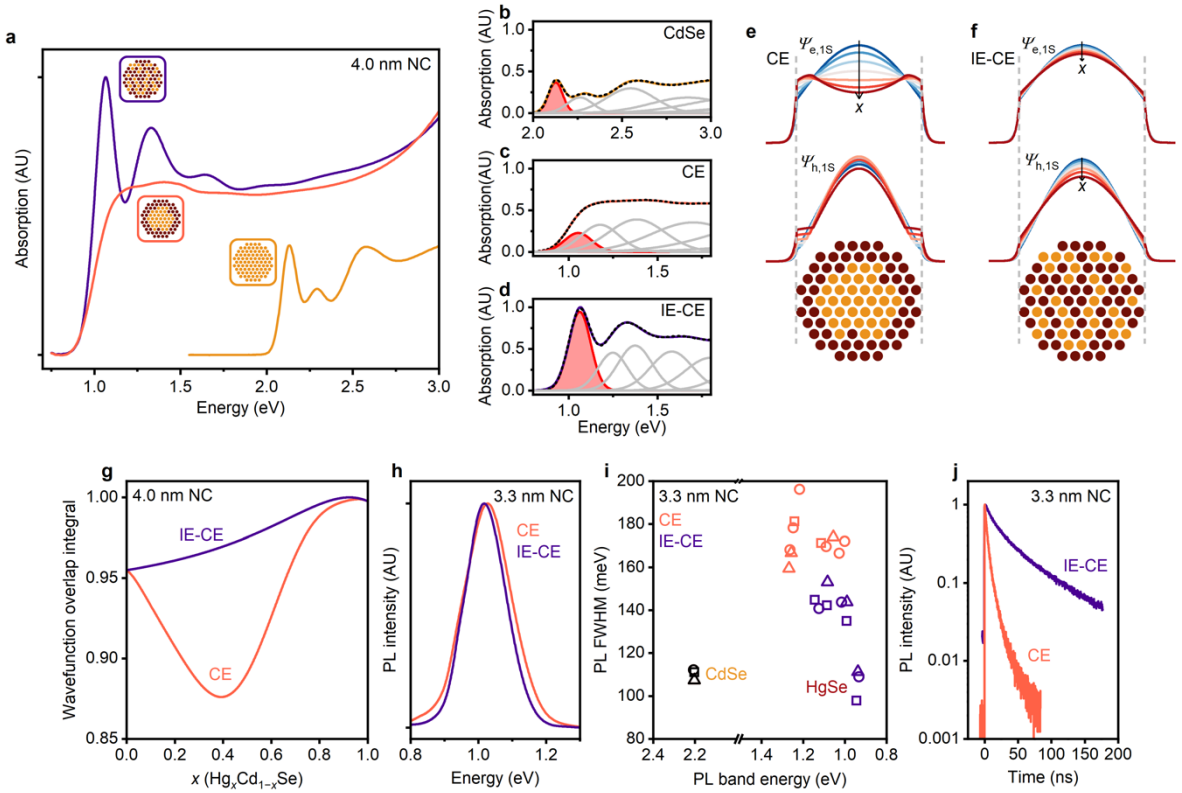

Figure 2. Dependence of photophysical properties on Hg^{2+} exchange mechanism in CdSe. (a) Absorption spectra of 4 nm CdSe NCs, CdSe/HgSe NCs produced by CE, and $Hg_xCd_{1-x}Se$ NCs produced by IE-CE. Spectra are plotted in arbitrary units (AU) and normalized by NC concentration. **(b-d)** Absorption spectra in (a) reconstructed as a sum of Gaussian functions (black dotted lines) reflecting individual electronic transitions (gray lines). Filled red curves indicate 1S−1S band transitions. **(e,f)** Effective mass approximation calculations of electron and hole wavefunctions of 4 nm NCs with total mercury composition of $0 \le x \le 0.6$ for (e) CdSe/HgSe NCs and (f) $Hg_xCd_{1-x}Se$ NCs. In CdSe/HgSe core/shell NCs, electron wavefunction is localized to the shell. **(g)** Wavefunction overlap integrals of 4.0 nm CdSe/HgSe NCs and $Hg_xCd_{1-x}Se$ NCs calculated by the effective mass approximation. **(h)** PL spectra of 3.3 nm CdSe/HgSe NCs and $Hg_xCd_{1-x}Se$ NCs with similar PL band energies. Spectra are normalized by maximum intensities. **(i)** PL FWHM of 3.3 nm NCs showing data from three replicate CE and IE-CE reactions. **(j)** PL decay of 3.3 nm CdSe/HgSe NCs and $Hg_xCd_{1-x}Se$ NCs. Intensity trends fit well to 2-component exponential decays as $A_1\exp(-t/\tau_1) + A_2\exp(-t/\tau_2)$ with A_1 = 83.5%, τ_1 = 3.8 ns, A_2 = 16.5 %, τ_2 = 14.2 ns for CdSe/HgSe NCs, and A_1 = 55.9%, τ_1 = 18.8 ns, A_2 = 44.1 %, τ_2 = 67.8 ns for $Hg_xCd_{1-x}Se$ NCs.

Dependence of photoluminescence on exchange mechanism. During the CE reaction, the PL full width at half maximum (FWHM) broadens relative to the CdSe NCs (**Figure 2h,i**). The CE products consistently exhibited broader FWHM (~167–196 meV) than those of IE-CE (~109–143 meV). These wider bandwidths for CE products are similar to those of previous CdSe/HgSe NCs[29,35] and CdSe-based cores with epitaxial HgS shells[36] and may

https://doi.org/10.26434/chemrxiv-2024-jx761 **ORCID:** https://orcid.org/0000-0002-0238-4816 Content not peer-reviewed by ChemRxiv. **License:** CC BY-NC-ND 4.0

result from scattering of strongly confined electrons in the shell by surface states and surface phonons[37] and/or inhomogeneity in faceting.[38] After complete conversion to HgSe through IE-CE, broadening fully disappears and the FWHM of HgSe products are as narrow as those of CdSe (**Table S4**). Homogeneous $Hg_xCd_{1-x}Se$ NCs exhibited a PL QY near 15–20% with a 2-component exponential decay with half-times of 18.8 ns and 67.8 ns (**Figure 2j**). In contrast, the CdSe/HgSe NCs exhibited a PL QY below 1% and rapid PL decay. These effects become more conspicuous with increasing NC sizes (**Figure S7**) and are consistent with electron trapping by surface states in CdSe/HgSe, as predicted by EMA calculations (**Figure 2e, Figure S8**).

Mechanism of interdiffusion enhancement. The CE and IE-CE reactions differ primarily by the rates of Hg^{2+}-Cd^{2+} interdiffusion, based on fittings of a Fickian diffusion model to the NC composition over time (**Supplementary Note 1**).[39] At 80 °C, IE-CE reaction dynamics fit well with a single Hg^{2+} diffusion coefficient (D) near ~10^{-22} m^2 s^{-1} (**Figure S9**) indicating that the surface exchange cation rate and the interdiffusion rate are equivalent. However, the model fit was a poor match to experimental data for CE reactions, as the surface reaction rate is much faster than the interdiffusion rate. This was even the case when modeling Fickian diffusion only over the time course after rapid exchange of surface Cd^{2+} atoms, indicating that the exchange rate decreases with progressive replacement of Cd^{2+} with Hg^{2+}, creating stable CdSe/HgSe structures, which is consistent with a reaction occurring at temperatures well below the alloying temperature.[28] We could more precisely evaluate the time course of exchange with slower reactions at room temperature in the absence of alkylthiol ligands (**Figure S10**), conditions at which D was 3 orders of magnitude smaller, resulting in core/shell NCs both with and without the Ag enhancer. In both cases, the initial burst of surface exchange rate was not impacted by Ag but did result in a ~4-fold increase in diffusion coefficient.

Role of Ag. Ag^+ diffuses in a CdSe lattice and occupies either interstitial sites (Ag_i) or substitutional sites for cadmium (Ag_{Cd}).[26,40-42] Two Ag_i sites together with a cation vacancy can form a charge-balanced “Frenkel defect” that rapidly diffuses to enhance the interdiffusion of Cd^{2+} and Hg^{2+} across vacancies. This mechanism predicts a dependence of

https://doi.org/10.26434/chemrxiv-2024-jx761 **ORCID:** https://orcid.org/0000-0002-0238-4816 Content not peer-reviewed by ChemRxiv. **License:** CC BY-NC-ND 4.0

exchange rate on Ag concentration[43,44] which we found to be true up to an amount of 0.075 Ag per Cd in the CdSe NC (**Figure S11**). With even larger amounts of the Ag reagent, the cation exchange rate decreased, PL bands broadened, and low energy absorption tails appeared (**Figure S12**) likely due to Ag_{Cd} clusters that form mid-gap states.[45]

The capacity of Ag^+ to catalyze Hg^{2+}-Cd^{2+} interdiffusion was also consistent with experiments applying CdSe/HgSe NCs purified from excess ions after a CE reaction. When Ag was added to the NCs at 80 °C, the absorption and emission spectra red-shifted, the 1S−1S absorption band sharpened and strengthened, and the PL band narrowed and increased in QY (**Figure 3**). There was no change in the absorption spectral features at energies well above the bandgap. These changes are consistent with interdiffusion-based shifts from a core/shell NC to a homogeneously alloyed NC without a change in overall composition. Because the PL spectra narrowed during alloying, the aforementioned broadening of CdSe/HgSe NC spectra must not be a result of population heterogeneity, indicating that CdSe/HgSe NCs intrinsically exhibit broader PL spectral bands than $Hg_xCd_{1-x}Se$ NCs.

https://doi.org/10.26434/chemrxiv-2024-jx761 **ORCID:** https://orcid.org/0000-0002-0238-4816 Content not peer-reviewed by ChemRxiv. **License:** CC BY-NC-ND 4.0

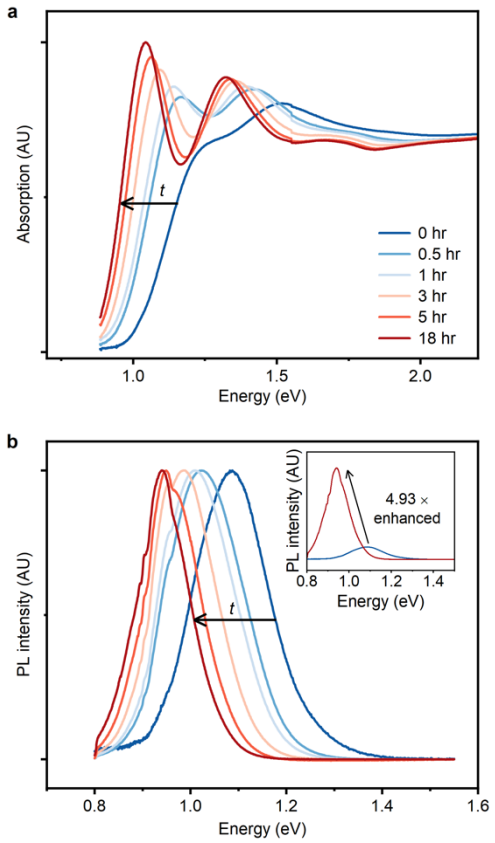

Figure 3. Interdiffusion-enhanced alloying of core/shell CdSe/HgSe NCs. After a CE reaction, CdSe/HgSe NCs were purified and reacted with the Ag reagent at 80 °C. Reaction time courses show changes in the **(a)** absorption spectrum and **(b)** PL spectrum. Both spectra are normalized by the maximum intensity. The inset in panel (b) shows the PL spectra before and after the reaction normalized by QY.

Role of ligands. Strongly binding alkanethiol ligands (dodecanethiol, DDT) play an essential role in IE-CE as soft Lewis bases that coordinate soft Hg^{2+} and Ag^{+} cations on the NC surface and in solution. These ligands tune the surface exchange rate and are also required for the colloidal stability of $Hg_xCd_{1-x}Se$ NCs. An equivalent amount of ~0.6–1.5 thiol per Cd in the NC is optimal for homogeneous alloying when applying equivalents of 1.5 Hg and 0.075 Ag. This quantity of ligand is balanced to exceed the amount required to completely passivate the NC surface but is insufficient to coordinate Hg^{2+} as unreactive dithiolate complexes. With increasing amounts of thiol, the exchange reaction decreases and almost no exchange reaction occurs in the presence of a large excess of the ligand (**Figure S13**). With low amounts of thiols insufficient to coordinate the NC surface, the absorption spectrum

https://doi.org/10.26434/chemrxiv-2024-jx761 **ORCID:** https://orcid.org/0000-0002-0238-4816 Content not peer-reviewed by ChemRxiv. **License:** CC BY-NC-ND 4.0

exhibits a weak 1S−1S transition and low PL QY similar to those of NCs exchanged without Ag, likely due to the fast surface reaction rate that yields a core/shell structure (**Figure S13**). However, after purification, the addition of thiol ligands increases the 1S−1S transition intensity and increases the PL QY more than 100-fold (**Figure S14**), indicating that thiols passivate the NC surface to prevent surface localized electrons from perturbation by surface states and/or surface phonons. Thiols further bind to Ag^+ in solution and reduce its reactivity to prevent heavy doping by Ag^+ (**Figure S12**). With the optimized amount of ligands, PL bandwidths are minimized and PL QY is maximized, and only a few Ag^+ per NC remain after exchange and can be easily extracted by the addition of trialkylphosphines (**Table S2**).

Homogeneous alloying across NC phase, shape, and composition. The IE-CE reaction can be applied to CdSe NCs with diverse structures to generate uniform HgSe and $Hg_xCd_{1-x}Se$ alloys that have not been generated through *de novo* synthetic methods. The hexagonal wurtzite phase of CdSe NCs can be obtained through colloidal synthesis processes using ligands such as alkylphosphonic acids.[46] As with cubic phase CdSe NCs, CE reactions on wurtzite CdSe NCs halted after ~3 hours and absorption features resembled those of cubic CdSe/HgSe NCs (**Figure 4a**), consistent with previous exchange reports.[47] These products exhibited much broader PL bands than their cubic counterparts (**Figure S15**) which may originate from the diverse facet types on wurtzite NCs. In contrast, with IE-CE, complete conversion to HgSe occurred while the crystal structure was retained (**Figure 4b, Table S5**), yielding a non-natural crystal form that has not been synthesized in pure form previously to our knowledge. The bandgap energy of both cubic and wurtzite HgSe NCs with equal sizes were similar and both exhibited narrow PL bands.

https://doi.org/10.26434/chemrxiv-2024-jx761 **ORCID:** https://orcid.org/0000-0002-0238-4816 Content not peer-reviewed by ChemRxiv. **License:** CC BY-NC-ND 4.0

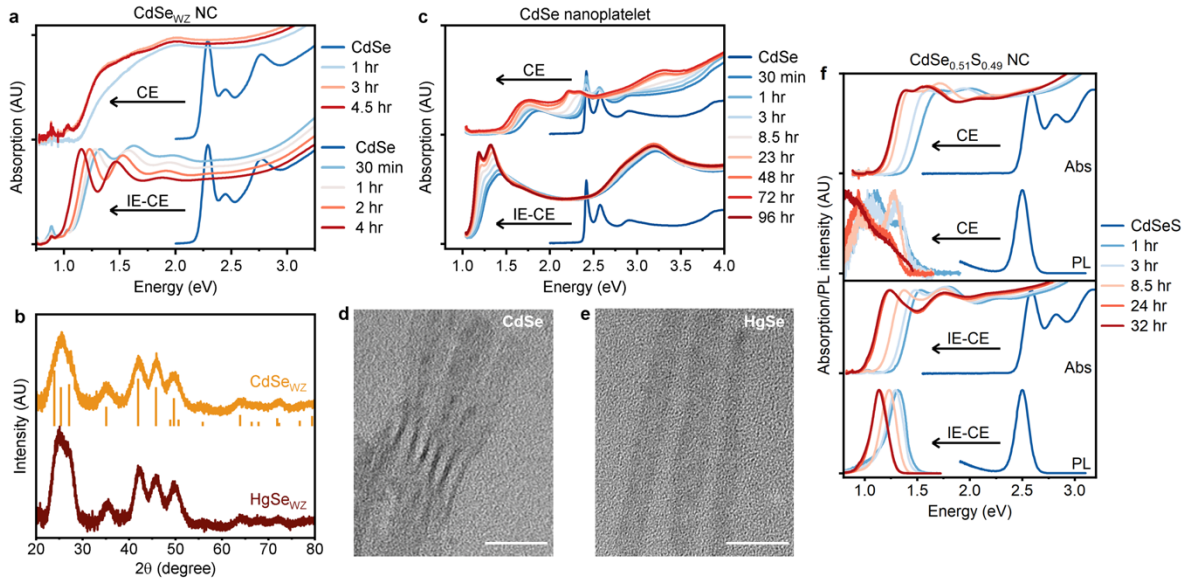

Figure 4. Interdiffusion-enhanced cation exchange (IE-CE) on cores with different crystal structure, shape, and composition. (a) Absorption spectra of wurtzite (WZ) CdSe NCs during CE (top) and IE-CE (bottom) normalized by the intensity of the 1S−1S band. **(b)** X-ray diffraction patterns of WZ CdSe NCs (orange) and their complete IE-CE products (brown). Orange vertical lines indicate bulk WZ CdSe. **(c)** Absorption spectra of 4.5 monolayer CdSe nanoplatelet during CE (top) and IE-CE (bottom), normalized by NC concentration. Transmission electron micrographs show **(d)** CdSe nanoplatelets and **(e)** their complete IE-CE products. Scale bars: 20 nm. **(f)** Absorption and PL spectra of $CdSe_{0.51}S_{0.49}$ NCs during CE (top) and IE-CE (bottom). Absorption and PL spectra are normalized by the maximum intensity of the 1S−1S band.

Mercury exchange reactions with CdSe NPLs were performed at room temperature or below due to the fragile morphology of these high surface area-to-volume ratio particles. As shown in **Figure 4c**, CE reactions of 4.5 ML-thick CdSe NPLs resulted in an immediate redshift of absorption bands, but with only small changes over the following 3 days. This has been observed previously,[27,48,49] and indicates that the diffusion of Hg^{2+} beyond 2 ML is hindered at room temperature. In contrast, the IE-CE process activates the diffusion of Hg^{2+} below the surface layers such that the absorption spectrum at 30 minutes is more red-shifted than that of the CE reaction after 3 days. As the reaction proceeds, two characteristic absorption peaks appear which are attributed to electronic transitions from heavy and light hole levels to the conduction band (**Figure S16**). Compared to the CdSe/HgSe NPLs deriving from CE, absorption intensities of HgSe NPLs are several times larger, with 4.6-fold larger molar extinction coefficients at 3.1 eV (400 nm) compared with CdSe NPLs (μ_{400} = 670,000 cm^{-1}).

https://doi.org/10.26434/chemrxiv-2024-jx761 **ORCID:** https://orcid.org/0000-0002-0238-4816 Content not peer-reviewed by ChemRxiv. **License:** CC BY-NC-ND 4.0

TEM revealed that the morphology was retained and elemental analysis revealed that exchange was ~98% complete and the original cation-to-anion ratio was maintained near 5:4 (**Figure 4d,e, Table S6**). CE reactions on $CdSe_xS_{1-x}$ and CdTe NCs also accelerated with the Ag enhancer (**Figure 4f**, **Figure S17**). In both cases, the PL bands became as narrow as those of the parent NCs. From telluride to selenide to sulfide, the cation exchange rate decreased in accord with an increase in bond strength, likely slowing diffusion of Ag^+. Complete conversion of CdTe NCs to HgTe NCs occurred through IE-CE at room temperature, whereas CdS NCs lacking selenium did not exhibit enhanced exchange with the Ag enhancer.

Infrared emitting core/shell NCs. Toward the generation of high-QY emitters with PL in the infrared, we optimized the growth of insulating homovalent CdZnS shells on HgSe and $Hg_xCd_{1-x}Se$ NCs prepared by IE-CE (**Figure 5a**). As anticipated with the similar crystalline lattices of CdSe and HgSe, similar benefits of PL QY enhancement and PL bandwidth narrowing were observed for HgSe and $Hg_xCd_{1-x}Se$ cores as for CdSe cores after deposition of CdZnS shells.[37] Before shell growth, trioctylphosphine extraction of residual Ag^+ was needed to prevent the diffusion of Hg^{2+} into the shell, which resulted in irreversible spectral blueshifts and broadening at elevated temperatures required for ZnS deposition (**Figure S18**). With Ag^+ extraction, shell growth temperatures below ~200 °C resulted in core/shell NCs with optical bandgaps slightly redshifted from those of the core (**Figure 5b-c, Figure S19**), which similarly occurs for CdSe-based cores. After shell growth, the NC size increased from 3.2 nm to 6.0 nm (**Figure 5d**) in agreement with the amount of shell precursors added. PL QY increased above 80%, and up to 91%, in the SWIR and the PL band narrowed to 102–139 meV FWHM (**Figure 5e, Figure S19, Table S5**). Core/shell nanocrystals based on HgSe NC cores exhibited the narrowest PL FWHMs, comparable to the most homogeneous PbS or PbSe NC cores and with comparable photophysical figures of merit as the commercial standards of visible spectrum NCs based on CdSe/CdZnS (**Figure 5e**). PL energy bands were tuned by composition while keeping the NC core size fixed. FWHM and QY values are summarized in **Figure 5f,g** in comparison with other infrared NCs reported to date.[9,11,29,35,50-75]

https://doi.org/10.26434/chemrxiv-2024-jx761 **ORCID:** https://orcid.org/0000-0002-0238-4816 Content not peer-reviewed by ChemRxiv. **License:** CC BY-NC-ND 4.0

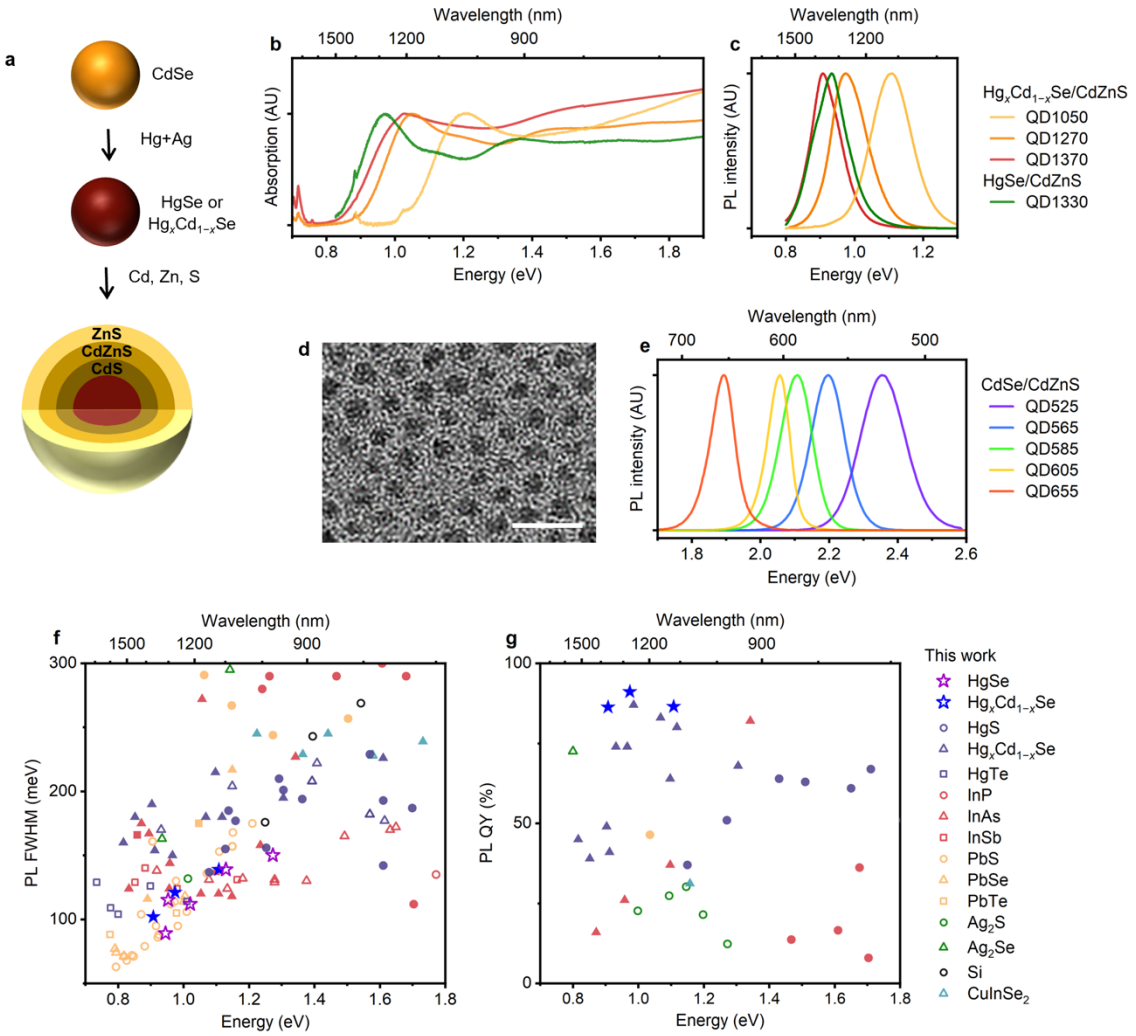

Figure 5. Characterization of core/shell HgSe/CdZnS and Hg$_x$Cd$_{1-x}$Se/CdZnS NCs deriving from IE-CE. (a) Schematic representation of synthesis process. **(b)** Absorption spectra of four NCs with indicated structures. 1S−1S band energies are tuned by different degrees of cation exchange. All cores are 3.2 nm and shells are composed of 0.8 ML CdS, 2.4 ML $Cd_{0.5}Zn_{0.5}S$, and 0.8 ML of ZnS. **(c)** PL spectra of four NCs with indicated structures. **(d)** Transmission electron micrograph of QD1270. **(e)** PL spectra of commercial visible spectrum CdSe/CdZnS NCs (Invitrogen) for comparison of bandwidths. **(f)** PL FWHM values for Hg$_x$Cd$_{1-x}$Se, HgSe, HgSe/CdZnS, and Hg$_x$Cd$_{1-x}$Se/CdZnS NCs (stars) in comparison with other core and core/shell NCs with PL between 700–1700 nm wavelength reported in the literature. **(g)** PL QY values for HgSe/CdZnS and Hg$_x$Cd$_{1-x}$Se/CdZnS NCs (stars) in comparison with other NCs with PL between 700–1700 nm wavelength reported in the literature. Open symbols in panels (f) and (g) indicate core NCs and filled symbols indicate core/shell NCs.

https://doi.org/10.26434/chemrxiv-2024-jx761 **ORCID:** https://orcid.org/0000-0002-0238-4816 Content not peer-reviewed by ChemRxiv. **License:** CC BY-NC-ND 4.0

Conclusion. In summary, we described a strategy to generate high-quality homogeneous binary and ternary NCs with infrared bandgaps. Using Ag enhancers with alkylthiol ligands, the cation interdiffusion rate and surface reaction rates can be balanced to achieve homogeneous mixing of cations across the NC. Unlike products with core/shell structures, the homogeneous alloys have enhanced exciton wavefunction overlap, which results in enhanced band edge absorbance and 1S−1S oscillator strength, high PL QY, and narrow PL linewidths. After deposition of CdZnS shells, the NCs exhibited both brighter and narrower PL than previous mercury chalcogenide-based NCs and other colloidal semiconductor NCs in the SWIR window, which can be explained by the enhanced confinement of electron and hole wavefunctions in the NC core and matching lattice structure to the CdZnS shell. With the diversity of crystal phases, shapes, and compositions now available in cadmium chalcogenides for applications in the visible spectrum, similar diversification of homogeneous and composition-tunable materials may now be readily obtainable in the infrared through IE-CE.

https://doi.org/10.26434/chemrxiv-2024-jx761 **ORCID:** https://orcid.org/0000-0002-0238-4816 Content not peer-reviewed by ChemRxiv. **License:** CC BY-NC-ND 4.0

Methods

Chemicals. Cadmium acetate dihydrate ($Cd(Ac)_2 \cdot 2H_2O$, 98%), cadmium oxide (CdO, ≥99.99%), mercury acetate ($Hg(Ac)_2$, ≥99.0%), silver nitrate ($AgNO_3$ >99%), sulfur (S, 99.98%), selenium (Se, 99.99%), tellurium (Te, 99.8%), selenium dioxide (SeO_2, ≥99.9%), 1-octadecene (ODE, 90%), oleic acid (OLAc, 90%), oleylamine (OLAm, 70%) tetramethylammonium hydroxide (TMAH, 25 wt% in methanol), stearic acid (95%), trioctylphosphine oxide (TOPO, 99%), 1,2-hexadecanediol (HDD, 90%), diphenylphosphine (DPP, 98%), 1-dodecanethiol (DDT, ≥98%), sodium hydroxide (NaOH, ≥98%) were purchased from Sigma Aldrich. *N*-tetradecylphosphonic acid (TDPA, >99%) was purchased from PCI Chemicals. Trioctylphosphine (TOP, 97%) was purchased from Strem Chemicals. Methanol (MeOH, ≥99.8%) was purchased from Macron Fine Chemicals. Acetone (99.5%), chloroform ($CHCl_3$, 99.8%), ethanol (EtOH, >95%), hexanes (98.5%), acetonitrile (99.9%), and toluene (99.5%) were purchased from Fisher Chemical. Myristic acid (99%) was purchased from Acros. Cadmium nitrate tetrahydrate ($Cd(NO_3)_2 \cdot 4H_2O$, 99.99%), zinc acetate ($Zn(Ac)_2$, 99.98%), tetrachloroethylene (TCE, 99+%), and octadecylphosphonic acid (ODPA, 97%) were purchased from Alfa Aesar. All chemicals were used without further purification.

Synthesis of precursors. *Cadmium stearate* (*$CdSt_2$*): $Cd(Ac)_2 \cdot 2H_2O$ (5 mmol) was dissolved in MeOH (250 mL) in a 1 L beaker. In a second 1 L beaker, stearic acid (12.5 mmol) was dissolved in a mixture of 350 mL MeOH, 37.5 mL $CHCl_3$, and 5.25 mL of TMAH solution. The cadmium solution is added dropwise to the stearic acid solution using a dropping funnel. The product was isolated by vacuum filtration and washed several times with MeOH. *Cadmium myristate* (*$CdMy_2$*)[76]: In a 1 L beaker, NaOH (15 mmol) and myristic acid (15 mmol) were dissolved in MeOH (0.5 L). In a 100 mL beaker, $CdNO_3 \cdot 4H_2O$ (5 mmol) was dissolved MeOH (50 mL). The cadmium solution was then added dropwise to the myristic acid solution with continuous stirring. The product was isolated by vacuum filtration and washed several times with MeOH. *Cd and Zn precursors for shell growth:* $Cd(Ac)_2$ or $Zn(Ac)_2$ (1 mmol) was dissolved in OLAm (10 mL) at 100 °C. *S precursor for shell growth:* S powder (1 mmol) was dissolved in ODE (10 mL) at 150 °C.

https://doi.org/10.26434/chemrxiv-2024-jx761 **ORCID:** https://orcid.org/0000-0002-0238-4816 Content not peer-reviewed by ChemRxiv. **License:** CC BY-NC-ND 4.0

Synthesis of zinc blende CdSe NCs. In a 50 mL three-neck flask, $CdSt_2$ (0.6 mmol), SeO_2 (0.6 mmol), HDD (0.6 mmol), and ODE (15 mL) were added and dried under vacuum at 100 °C for one hour. The solution was then rapidly heated to 230 °C under nitrogen at a rate of 20 °C/min (to yield 3.2 nm CdSe NCs). The temperature was maintained for 15 minutes and the reaction mixture was rapidly cooled by removing the heating mantle. At ~110 °C, 3 mL of OLAc was injected to prevent precipitation of the NCs. The size was selected by controlling the reaction temperature and growth time. For purification, the crude solution is diluted with an equal volume of hexanes and 1.5 mL of this solution is mixed with 35 mL MeOH and 5 mL acetone. After centrifugation, precipitates were dissolved in 1.5 mL hexanes. Precipitation with MeOH/acetone is repeated two more times before the products are finally dispersed in hexanes.

Synthesis of wurtzite CdSe.[46] CdO (60 mg), ODPA (280 mg), and TOPO (3.0 g) were added to a three-necked flask and heated to 300 °C under nitrogen until the solution became colorless and transparent. Then, TOP (1.5 g) was injected and the solution was heated to 380 °C. A selenium solution prepared by dissolving Se powder (58 mg) in TOP (360 mg) was injected into the cadmium solution and the heating mantle was immediately removed. The NCs were diluted with toluene, precipitated twice with MeOH, and finally dissolved in toluene.

Synthesis of $CdSe_{0.51}S_{0.49}$ NCs. CdO (0.2 mmol), stearic acid (0.6 mmol), and ODE (10 mL) were added to a three-necked flask and heated to 270 °C under nitrogen until the solution become colorless and transparent. Then, a mixture of ODE-S (0.1 M; 0.5 mL) and Se suspended in ODE (0.1 M; 0.5 mL) was injected. After the injection the temperature was set at 260 °C and for 5 minutes. The NCs were purified using the same process used for zinc blende CdSe NCs.

Synthesis of CdTe NCs. CdO (12.8 mg, 0.1 mmol), TDPA (61 mg, 0.22 mmol) and ODE (5 mL) were added to a three-necked flask and heated under nitrogen to 300 °C until the solution became colorless and transparent. After cooling to room temperature, OLAm (0.5 mL) was added and the solution was heated to 300°C under nitrogen. A tellurium solution was prepared by dissolving Te powder (12.76 mg, 0.1 mmol) in ODE (5 mL) and TOP (1 mL)

https://doi.org/10.26434/chemrxiv-2024-jx761 **ORCID:** https://orcid.org/0000-0002-0238-4816 Content not peer-reviewed by ChemRxiv. **License:** CC BY-NC-ND 4.0

at ~280°C. After cooling to room temperature, DPP (5 µL) in OLAm (45 µL) was added to the tellurium solution. The tellurium solution (3 mL) was then injected into the cadmium solution and the temperature was set to 250°C for 10 minutes. The reaction mixture was then cooled to room temperature, diluted an equal volume of hexanes, and centrifuged to remove unreacted white precursors. The NCs were purified by repeated extraction with hexanes-MeOH, and finally dissolved in hexanes and stored at 4 °C under an inert atmosphere.

Synthesis of 4.5 ML CdSe NPLs. In a 50 mL three-neck flask, $Cd(My)_2$ (340 mg), Se (24 mg), and ODE (25 mL) were degassed for 30 minutes at room temperature. Under nitrogen flow, the temperature was then raised to 240 °C. When the mixture reached 220 °C, $Cd(Ac)_2 \cdot 2H_2O$ (100 mg) was added and the reaction was stopped after 10 min at 240 °C. The NPLs were diluted with hexanes (30 mL) and precipitated with EtOH (30 mL). The NPLs were finally suspended in hexanes (10 mL).

Mercury cation exchange. In a typical reaction, zinc blende CdSe NCs (100 nmol) dispersed in ODE (8 mL) were mixed with 100 equivalents of OLAm and 0.6–1.5 equivalents of DDT relative to the number of Cd ions in the NCs. A mercury precursor solution (0.1 M) was prepared by dissolving $Hg(Ac_2)$ in OLAm at 50 °C for one hour. A silver precursor solution (0.02 M) was prepared by dissolving $AgNO_3$ in OLAm by sonication at room temperature. The CdSe solution was heated to 80 °C and a mixture of Hg and Ag precursor solutions was rapidly injected. Typically, 1.5 equivalents of Hg ions and 0.075 equivalents of Ag ions per Cd ions was used. The cation exchange reaction was monitored by UV-VIS-NIR absorption spectroscopy. The NCs were purified using the same process used for zinc blende CdSe NCs.The same protocol was used for cation exchange of wurtzite CdSe NCs, $CdSe_{0.51}S_{0.49}$ NCs, CdTe NCs, and CdSe NPLs with the exception that CdTe NCs and CdSe NPLs were reacted at room temperature and no thiol ligands were applied.

Ag extraction. HgSe or $Hg_xCd_{1-x}Se$ NCs (50 nmol) were dissolved in ODE (4 mL), OLAc (0.2 mL), and OLAm (0.1 mL). The solution was heated to 50 °C and TOP (50 µL) was injected. After 2 hours, NCs were purified twice and finally dissolved in hexanes. Before purification, the crude solution is diluted with an equal volume of hexanes and 1 mL of OLAc and OLAm is added to prevent the complete stripping of ligands during the purification. 1.5

https://doi.org/10.26434/chemrxiv-2024-jx761 **ORCID:** https://orcid.org/0000-0002-0238-4816 Content not peer-reviewed by ChemRxiv. **License:** CC BY-NC-ND 4.0

mL of this solution is mixed with 35 mL MeOH and 5 mL acetone for precipitation. After two times of precipitation, precipitates were dissolved in hexanes.

Shell growth. For a typical reaction, $Hg_xCd_{1-x}Se$ NCs (100 nmol) were dissolved in ODE (6 mL) and OLAm (2 mL) and heated to 50 °C. In all cases, shells were grown in 0.8 ML increments by dropwise addition of the S precursor followed by the Cd/Zn precursor. The growth of the first S layer was initiated at 50 °C. After 10 min, the NC solution was heated to 120 °C, and the Cd precursor was added and allowed to react for 10 min. The reaction temperature was raised in 10 °C increments between each precursor addition until reaching a maximum of 200 °C. Typically, 0.8 ML of CdS, 2.4 ML of $Cd_{0.5}Zn_{0.5}S$, and 0.8 ML of ZnS were successively overcoated. After the reaction, NCs were purified by precipitation with MeOH and acetone three times and finally dispersed in hexanes.

Instrumentation. TEM images and EDS data were obtained using a JEOL JEM-2100F and JEOL 2010 LaB6. Powder XRD patterns were obtained using a Bruker D8 ADVANCE. ICP-OES was performed using a PerkinElmer Optima 8300. Absorption spectra were obtained using an Agilent Cary 5000 UV-Vis-NIR spectrophotometer. PL spectra were obtained using a Horiba NanoLog fluorometer. PL lifetime was measured at room temperature with a home-built single-photon-counting spectroscopy setup at the Materials Research Laboratory at UIUC.

Spectral decomposition and transition oscillator strength determination. A Gaussian mixture model was fit to energy-scaled absorption spectra, $A(E)$, obtained from NC suspensions with experimentally measured concentration and diameter as previously described,[34] with

$$A(E) = \sum_{i=1}^{n} \frac{a_i}{2\sqrt{2\pi}\, dR\, (E_i - E_g)} \exp\left[-\frac{(E - E_g)^2}{8\, dR^2\, (E_i - E_g)^2}\right] \quad (1)$$

where each Gaussian function i has area a_i and centroid energy E_i, dR is the relative standard deviation of NC radius, and E_g is the bulk bandgap energy. To calculate E_g for CdSe/HgSe and $Hg_xCd_{1-x}Se$, a linear interpolation between the bandgaps of CdSe (1.74 eV) and HgSe (–0.06 eV) was applied based on the total NC composition *x*. The values a_i, E_i,

https://doi.org/10.26434/chemrxiv-2024-jx761 **ORCID:** https://orcid.org/0000-0002-0238-4816 Content not peer-reviewed by ChemRxiv. **License:** CC BY-NC-ND 4.0

and dR were fitting parameters with initial guesses for E_i and the number of transitions n determined from minima of the second derivative of $A(E)$. E_i values were fixed within ±50 meV of initial guesses while a_i and dR were unbounded. The models were fit using the least squares method in Matlab. The values of a_i were proportional to oscillator strength when the nanocrystal size is fixed,[34] and only relative values were determined.

EMA calculations. NCs were modeled as spherically symmetric concentric layers with finite potential energy for non-interacting electrons and holes by the method of Haus *et al*.[77] and described further for the CdTe/HgTe and $Hg_xCd_{1-x}Te$ systems by Smith *et al*.[34] The time-independent Schrödinger equation in three dimensions was solved to calculate the kinetic energies and normalized wavefunctions of the electron (ψ_e) and hole (ψ_h) and the bandgap energy was calculated with inclusion of a Coulombic term as a perturbation. For $Hg_xCd_{1-x}Se$ alloy domains, a linear interpolation between materials parameters of CdSe and HgSe was applied based on the NC composition *x*, including for the electron effective masses ($m_{\mathrm{e,CdSe}} = 0.112$, $m_{\mathrm{e,HgSe}} = 0.042$), hole effective masses ($m_{\mathrm{h,CdSe}} = 0.469$, $m_{\mathrm{h,HgSe}} = 0.019$), dielectric constants ($\varepsilon_{\infty,\mathrm{CdSe}} = 6.2$, $\varepsilon_{\infty,\mathrm{HgSe}} = 16.5$), electronic bandgaps, conduction band offsets ($\Delta E_{\mathrm{C,CdSe}} = -1.36$ eV, $\Delta E_{\mathrm{C,HgSe}} = -2.69$ eV), valence band offsets ($\Delta E_{\mathrm{V,CdSe}} = 0.60$ eV, $\Delta E_{\mathrm{V,HgSe}} = 1.07$ eV), and cubic lattice parameters a_c. The total wavefunction overlap ϕ_total was calculated as

$$\phi_\mathrm{total} = \int_0^\infty 4\pi r^2 \psi_\mathrm{e} \psi_\mathrm{h} dr \tag{2}$$

where r is the radial distance from the NC center. The surface electronic wavefunction localization $\phi_\mathrm{e,surf}$ was calculated as the integrated radial distribution function starting from approximately one atomic layer from the surface of a NC with radius r_NC as

$$\phi_\mathrm{e,surf} = \int_{r_\mathrm{NC}-a_\mathrm{c}/4}^\infty 4\pi r^2 \psi_e^2 dr \tag{3}$$

PL QY calculation. For QY measurements, NCs were dispersed in TCE and diluted so that the absorption was ~0.05 at 700 nm. Relative QY was measured with respect to indocyanine green (in DMSO, QY = 13%) under 700 nm excitation.

https://doi.org/10.26434/chemrxiv-2024-jx761 **ORCID:** https://orcid.org/0000-0002-0238-4816 Content not peer-reviewed by ChemRxiv. **License:** CC BY-NC-ND 4.0

Absorption coefficient calculation. The molar absorption coefficients of CdSe NCs were calculated based on the reported correlations between the size and 1S−1S band energy. The molar absorption coefficient of $Hg_xCd_{1-x}Se$ NCs and $Hg_xCd_{1-x}Se$/CdZnS NCs were calculated by assuming the number of NCs did not change during the IE-CE reaction and shell overcoating process. The intrinsic absorption coefficient (μ) was derived from the absorbance (A) of the NC solution as:

$$\mu = \frac{\ln(10)\, A}{f_V L} \tag{4}$$

where f_V is the volume fraction of NCs in solution and L is the optical path length of the cuvette (1 cm).

Acknowledgements. This work was supported by funds from the National Institutes of Health (R01CA227699, R01GM131272, R01EB032249, R01EB032725) and the National Science Foundation (2232681).

https://doi.org/10.26434/chemrxiv-2024-jx761 **ORCID:** https://orcid.org/0000-0002-0238-4816 Content not peer-reviewed by ChemRxiv. **License:** CC BY-NC-ND 4.0

REFERENCES

1 García de Arquer, F. P., Talapin, D. V., Klimov, V. I., Arakawa, Y., Bayer, M. & Sargent, E. H. Semiconductor quantum dots: Technological progress and future challenges. *Science* **373**, eaaz8541 (2021).

2 Murray, C. B., Norris, D. J. & Bawendi, M. G. Synthesis and characterization of nearly monodisperse CdE (E = sulfur, selenium, tellurium) semiconductor nanocrystallites. *Journal of the American Chemical Society* **115**, 8706-8715 (1993).

3 Kim, J. Y., Voznyy, O., Zhitomirsky, D. & Sargent, E. H. 25th Anniversary Article: Colloidal Quantum Dot Materials and Devices: A Quarter-Century of Advances. *Advanced Materials* **25**, 4986-5010 (2013).

4 Pietryga, J. M., Park, Y.-S., Lim, J., Fidler, A. F., Bae, W. K., Brovelli, S. & Klimov, V. I. Spectroscopic and Device Aspects of Nanocrystal Quantum Dots. *Chemical Reviews* **116**, 10513-10622 (2016).

5 Jang, E. & Jang, H. Review: Quantum Dot Light-Emitting Diodes. *Chemical Reviews* **123**, 4663-4692 (2023).

6 Park, J., Jayaraman, A., Schrader, A. W., Hwang, G. W. & Han, H.-S. Controllable modulation of precursor reactivity using chemical additives for systematic synthesis of high-quality quantum dots. *Nature Communications* **11**, 5748 (2020).

7 Vasilopoulou, M., Fakharuddin, A., García de Arquer, F. P., Georgiadou, D. G., Kim, H., Mohd Yusoff, A. R. b., Gao, F., Nazeeruddin, M. K., Bolink, H. J. & Sargent, E. H. Advances in solution-processed near-infrared light-emitting diodes. *Nature Photonics* **15**, 656-669 (2021).

8 Yang, Y., Jiang, Q. & Zhang, F. Nanocrystals for Deep-Tissue In Vivo Luminescence Imaging in the Near-Infrared Region. *Chemical Reviews* **124**, 554-628 (2024).

9 Franke, D., Harris, D. K., Chen, O., Bruns, O. T., Carr, J. A., Wilson, M. W. B. & Bawendi, M. G. Continuous injection synthesis of indium arsenide quantum dots emissive in the short-wavelength infrared. *Nature Communications* **7**, 12749 (2016).

10 Janke, E. M., Williams, N. E., She, C., Zherebetskyy, D., Hudson, M. H., Wang, L., Gosztola, D. J., Schaller, R. D., Lee, B., Sun, C., Engel, G. S. & Talapin, D. V. Origin of Broad Emission Spectra in InP Quantum Dots: Contributions from Structural and Electronic Disorder. *Journal of the American Chemical Society* **140**, 15791-15803 (2018).

11 Hendricks, M. P., Campos, M. P., Cleveland, G. T., Jen-La Plante, I. & Owen, J. S. A tunable library of substituted thiourea precursors to metal sulfide nanocrystals. *Science* **348**, 1226-1230 (2015).

12 Campos, M. P., Hendricks, M. P., Beecher, A. N., Walravens, W., Swain, R. A., Cleveland, G. T., Hens, Z., Sfeir, M. Y. & Owen, J. S. A Library of Selenourea Precursors to PbSe Nanocrystals with Size Distributions near the Homogeneous Limit. *Journal of the American Chemical Society* **139**, 2296-2305 (2017).

13 Peng, X., Abelson, A., Wang, Y., Qian, C., Shangguan, J., Zhang, Q., Yu, L., Yin, Z.-W., Zheng, W., Bustillo, K. C., Guo, X., Liao, H.-G., Sun, S.-G., Law, M. & Zheng, H. In Situ TEM Study of the Degradation of PbSe Nanocrystals in Air. *Chemistry of Materials* **31**, 190-199 (2019).

https://doi.org/10.26434/chemrxiv-2024-jx761 **ORCID:** https://orcid.org/0000-0002-0238-4816 Content not peer-reviewed by ChemRxiv. **License:** CC BY-NC-ND 4.0

14 Beygi, H., Sajjadi, S. A., Babakhani, A., Young, J. F. & van Veggel, F. C. J. M. Surface chemistry of as-synthesized and air-oxidized PbS quantum dots. *Applied Surface Science* **457**, 1-10 (2018).
15 Gréboval, C., Chu, A., Goubet, N., Livache, C., Ithurria, S. & Lhuillier, E. Mercury Chalcogenide Quantum Dots: Material Perspective for Device Integration. *Chemical Reviews* **121**, 3627-3700 (2021).
16 Lu, H., Carroll, G. M., Neale, N. R. & Beard, M. C. Infrared Quantum Dots: Progress, Challenges, and Opportunities. *ACS Nano* **13**, 939-953 (2019).
17 Deng, Z., Jeong, K. S. & Guyot-Sionnest, P. Colloidal Quantum Dots Intraband Photodetectors. *ACS Nano* **8**, 11707-11714 (2014).
18 Kamath, A., Melnychuk, C. & Guyot-Sionnest, P. Toward Bright Mid-Infrared Emitters: Thick-Shell n-Type HgSe/CdS Nanocrystals. *Journal of the American Chemical Society* **143**, 19567-19575 (2021).
19 Kamath, A., Schaller, R. D. & Guyot-Sionnest, P. Bright Fluorophores in the Second Near-Infrared Window: HgSe/CdSe Quantum Dots. *Journal of the American Chemical Society* **145**, 10809-10816 (2023).
20 Madejczyk, P., Manyk, T. & Rutkowski, J. Research on Electro-Optical Characteristics of Infrared Detectors with HgCdTe Operating at Room Temperature. *Sensors* **23**, 1088 (2023).
21 Smith, A. M. & Nie, S. Bright and Compact Alloyed Quantum Dots with Broadly Tunable Near-Infrared Absorption and Fluorescence Spectra through Mercury Cation Exchange. *Journal of the American Chemical Society* **133**, 24-26 (2011).
22 De Trizio, L. & Manna, L. Forging Colloidal Nanostructures via Cation Exchange Reactions. *Chemical Reviews* **116**, 10852-10887 (2016).
23 Groeneveld, E., Witteman, L., Lefferts, M., Ke, X., Bals, S., Van Tendeloo, G. & de Mello Donega, C. Tailoring ZnSe–CdSe Colloidal Quantum Dots via Cation Exchange: From Core/Shell to Alloy Nanocrystals. *ACS Nano* **7**, 7913-7930 (2013).
24 Koscher, B. A., Bronstein, N. D., Olshansky, J. H., Bekenstein, Y. & Alivisatos, A. P. Surface- vs Diffusion-Limited Mechanisms of Anion Exchange in CsPbBr3 Nanocrystal Cubes Revealed through Kinetic Studies. *Journal of the American Chemical Society* **138**, 12065-12068 (2016).
25 Ma, F., Abboud, K. A. & Zeng, C. Precision synthesis of a CdSe semiconductor nanocluster via cation exchange. *Nature Synthesis* **2**, 949-959 (2023).
26 Dutt, M. & Sharma, B. 3 Diffusion in compound semiconductors. *Diffusion in Semiconductors*, 1-63 (1998).
27 Izquierdo, E., Robin, A., Keuleyan, S., Lequeux, N., Lhuillier, E. & Ithurria, S. Strongly Confined HgTe 2D Nanoplatelets as Narrow Near-Infrared Emitters. *Journal of the American Chemical Society* **138**, 10496-10501 (2016).
28 Shen, G. & Guyot-Sionnest, P. HgTe/CdTe and HgSe/CdX (X = S, Se, and Te) Core/Shell Mid-Infrared Quantum Dots. *Chemistry of Materials* **31**, 286-293 (2019).
29 Sarkar, S., Le, P., Geng, J., Liu, Y., Han, Z., Zahid, M. U., Nall, D., Youn, Y., Selvin, P. R. & Smith, A. M. Short-Wave Infrared Quantum Dots with Compact Sizes as Molecular Probes for Fluorescence Microscopy. *Journal of the American Chemical Society* **142**, 3449-3462 (2020).

https://doi.org/10.26434/chemrxiv-2024-jx761 **ORCID:** https://orcid.org/0000-0002-0238-4816 Content not peer-reviewed by ChemRxiv. **License:** CC BY-NC-ND 4.0

30 Choi, D., Yoon, B., Kim, D.-K., Baik, H., Choi, J.-H. & Jeong, K. S. Major Electronic Transition Shift from Bandgap to Localized Surface Plasmon Resonance in CdxHg1–xSe Alloy Nanocrystals. *Chemistry of Materials* **29**, 8548-8554 (2017).

31 Moreels, I., Lambert, K., Smeets, D., De Muynck, D., Nollet, T., Martins, J. C., Vanhaecke, F., Vantomme, A., Delerue, C., Allan, G. & Hens, Z. Size-Dependent Optical Properties of Colloidal PbS Quantum Dots. *ACS Nano* **3**, 3023-3030 (2009).

32 Moreels, I., Lambert, K., De Muynck, D., Vanhaecke, F., Poelman, D., Martins, J. C., Allan, G. & Hens, Z. Composition and Size-Dependent Extinction Coefficient of Colloidal PbSe Quantum Dots. *Chemistry of Materials* **19**, 6101-6106 (2007).

33 Massiot, I., Cattoni, A. & Collin, S. Progress and prospects for ultrathin solar cells. *Nature Energy* **5**, 959-972 (2020).

34 Smith, A. M., Lane, L. A. & Nie, S. Mapping the spatial distribution of charge carriers in quantum-confined heterostructures. *Nature Communications* **5**, 4506 (2014).

35 Lee, G., Jeong, W. H., Kim, B., Jeon, S., Smith, A. M., Seo, J., Suzuki, K., Kim, J.-y., Lee, H., Choi, H., Chung, D. S., Choi, J., Choi, H. & Lim, S. J. Design and Synthesis of CdHgSe/HgS/CdZnS Core/Multi-Shell Quantum Dots Exhibiting High-Quantum-Yield Tissue-Penetrating Shortwave Infrared Luminescence. *Small* **19**, 2301161 (2023).

36 Sayevich, V., Robinson, Z. L., Kim, Y., Kozlov, O. V., Jung, H., Nakotte, T., Park, Y.-S. & Klimov, V. I. Highly versatile near-infrared emitters based on an atomically defined HgS interlayer embedded into a CdSe/CdS quantum dot. *Nature Nanotechnology* **16**, 673-679 (2021).

37 Cui, J., Beyler, A. P., Coropceanu, I., Cleary, L., Avila, T. R., Chen, Y., Cordero, J. M., Heathcote, S. L., Harris, D. K., Chen, O., Cao, J. & Bawendi, M. G. Evolution of the Single-Nanocrystal Photoluminescence Linewidth with Size and Shell: Implications for Exciton–Phonon Coupling and the Optimization of Spectral Linewidths. *Nano Letters* **16**, 289-296 (2016).

38 Nguyen, H. A. *et al.* Design Rules for Obtaining Narrow Luminescence from Semiconductors Made in Solution. *Chemical Reviews* **123**, 7890-7952 (2023).

39 Gupta, A., Ondry, J. C., Chen, M., Hudson, M. H., Coropceanu, I., Sarma, N. A. & Talapin, D. V. Diffusion-Limited Kinetics of Isovalent Cation Exchange in III–V Nanocrystals Dispersed in Molten Salt Reaction Media. *Nano Letters* **22**, 6545-6552 (2022).

40 Sahu, A., Kang, M. S., Kompch, A., Notthoff, C., Wills, A. W., Deng, D., Winterer, M., Frisbie, C. D. & Norris, D. J. Electronic Impurity Doping in CdSe Nanocrystals. *Nano Letters* **12**, 2587-2594 (2012).

41 Ott, F. D., Spiegel, L. L., Norris, D. J. & Erwin, S. C. Microscopic Theory of Cation Exchange in CdSe Nanocrystals. *Physical Review Letters* **113**, 156803 (2014).

42 Kompch, A., Sahu, A., Notthoff, C., Ott, F., Norris, D. J. & Winterer, M. Localization of Ag Dopant Atoms in CdSe Nanocrystals by Reverse Monte Carlo Analysis of EXAFS Spectra. *The Journal of Physical Chemistry C* **119**, 18762-18772 (2015).

43 Casavola, M., van Huis, M. A., Bals, S., Lambert, K., Hens, Z. & Vanmaekelbergh, D. Anisotropic Cation Exchange in PbSe/CdSe Core/Shell Nanocrystals of Different Geometry. *Chemistry of Materials* **24**, 294-302 (2012).

44 Cahen, D. & Lubomirsky, I. Percolation-Controlled Semiconductor Doping. *Chemistry of Materials* **10**, 2596-2598 (1998).

https://doi.org/10.26434/chemrxiv-2024-jx761 **ORCID:** https://orcid.org/0000-0002-0238-4816 Content not peer-reviewed by ChemRxiv. **License:** CC BY-NC-ND 4.0

45 Yang, L., Knowles, K. E., Gopalan, A., Hughes, K. E., James, M. C. & Gamelin, D. R. One-Pot Synthesis of Monodisperse Colloidal Copper-Doped CdSe Nanocrystals Mediated by Ligand–Copper Interactions. *Chemistry of Materials* **28**, 7375-7384 (2016).

46 Carbone, L., Nobile, C., De Giorgi, M., Sala, F. D., Morello, G., Pompa, P., Hytch, M., Snoeck, E., Fiore, A., Franchini, I. R., Nadasan, M., Silvestre, A. F., Chiodo, L., Kudera, S., Cingolani, R., Krahne, R. & Manna, L. Synthesis and Micrometer-Scale Assembly of Colloidal CdSe/CdS Nanorods Prepared by a Seeded Growth Approach. *Nano Letters* **7**, 2942-2950 (2007).

47 Dumett Torres, D., Banerjee, P., Pamidighantam, S. & Jain, P. K. A Non-Natural Wurtzite Polymorph of HgSe: A Potential 3D Topological Insulator. *Chemistry of Materials* **29**, 6356-6366 (2017).

48 Dabard, C. *et al.* Optimized Cation Exchange for Mercury Chalcogenide 2D Nanoplatelets and Its Application for Alloys. *Chemistry of Materials* **33**, 9252-9261 (2021).

49 Izquierdo, E., Dufour, M., Chu, A., Livache, C., Martinez, B., Amelot, D., Patriarche, G., Lequeux, N., Lhuillier, E. & Ithurria, S. Coupled HgSe Colloidal Quantum Wells through a Tunable Barrier: A Strategy To Uncouple Optical and Transport Band Gap. *Chemistry of Materials* **30**, 4065-4072 (2018).

50 Yadav, R., Kwon, Y., Rivaux, C., Saint-Pierre, C., Ling, W. L. & Reiss, P. Narrow Near-Infrared Emission from InP QDs Synthesized with Indium(I) Halides and Aminophosphine. *Journal of the American Chemical Society* **145**, 5970-5981 (2023).

51 Dennis, A. M., Mangum, B. D., Piryatinski, A., Park, Y.-S., Hannah, D. C., Casson, J. L., Williams, D. J., Schaller, R. D., Htoon, H. & Hollingsworth, J. A. Suppressed Blinking and Auger Recombination in Near-Infrared Type-II InP/CdS Nanocrystal Quantum Dots. *Nano Letters* **12**, 5545-5551 (2012).

52 Saeboe, A. M., Nikiforov, A. Y., Toufanian, R., Kays, J. C., Chern, M., Casas, J. P., Han, K., Piryatinski, A., Jones, D. & Dennis, A. M. Extending the Near-Infrared Emission Range of Indium Phosphide Quantum Dots for Multiplexed In Vivo Imaging. *Nano Letters* **21**, 3271-3279 (2021).

53 Srivastava, V., Dunietz, E., Kamysbayev, V., Anderson, J. S. & Talapin, D. V. Monodisperse InAs Quantum Dots from Aminoarsine Precursors: Understanding the Role of Reducing Agent. *Chemistry of Materials* **30**, 3623-3627 (2018).

54 Srivastava, V., Janke, E. M., Diroll, B. T., Schaller, R. D. & Talapin, D. V. Facile, Economic and Size-Tunable Synthesis of Metal Arsenide Nanocrystals. *Chemistry of Materials* **28**, 6797-6802 (2016).

55 Ginterseder, M., Franke, D., Perkinson, C. F., Wang, L., Hansen, E. C. & Bawendi, M. G. Scalable Synthesis of InAs Quantum Dots Mediated through Indium Redox Chemistry. *Journal of the American Chemical Society* **142**, 4088-4092 (2020).

56 Liu, W., Chang, A. Y., Schaller, R. D. & Talapin, D. V. Colloidal InSb Nanocrystals. *Journal of the American Chemical Society* **134**, 20258-20261 (2012).

57 Busatto, S., de Ruiter, M., Jastrzebski, J. T. B. H., Albrecht, W., Pinchetti, V., Brovelli, S., Bals, S., Moret, M.-E. & de Mello Donega, C. Luminescent Colloidal InSb Quantum Dots from In Situ Generated Single-Source Precursor. *ACS Nano* **14**, 13146-13160 (2020).

58 Weidman, M. C., Beck, M. E., Hoffman, R. S., Prins, F. & Tisdale, W. A. Monodisperse, Air-Stable PbS Nanocrystals via Precursor Stoichiometry Control. *ACS Nano* **8**, 6363-6371 (2014).

https://doi.org/10.26434/chemrxiv-2024-jx761 **ORCID:** https://orcid.org/0000-0002-0238-4816 Content not peer-reviewed by ChemRxiv. **License:** CC BY-NC-ND 4.0

59 Pietryga, J. M., Werder, D. J., Williams, D. J., Casson, J. L., Schaller, R. D., Klimov, V. I. & Hollingsworth, J. A. Utilizing the Lability of Lead Selenide to Produce Heterostructured Nanocrystals with Bright, Stable Infrared Emission. *J. Am. Chem. Soc.* **130**, 4879-4885 (2008).

60 Kovalenko, M. V., Schaller, R. D., Jarzab, D., Loi, M. A. & Talapin, D. V. Inorganically Functionalized PbS–CdS Colloidal Nanocrystals: Integration into Amorphous Chalcogenide Glass and Luminescent Properties. *Journal of the American Chemical Society* **134**, 2457-2460 (2012).

61 Kovalenko, M. V., Talapin, D. V., Loi, M. A., Cordella, F., Hesser, G., Bodnarchuk, M. I. & Heiss, W. Quasi-Seeded Growth of Ligand-Tailored PbSe Nanocrystals through Cation-Exchange-Mediated Nucleation. *Angewandte Chemie* **120**, 3071-3075 (2008).

62 Yu, W. W., Falkner, J. C., Shih, B. S. & Colvin, V. L. Preparation and Characterization of Monodisperse PbSe Semiconductor Nanocrystals in a Noncoordinating Solvent. *Chemistry of Materials* **16**, 3318-3322 (2004).

63 Abel, K. A., Qiao, H., Young, J. F. & van Veggel, F. C. J. M. Four-Fold Enhancement of the Activation Energy for Nonradiative Decay of Excitons in PbSe/CdSe Core/Shell versus PbSe Colloidal Quantum Dots. *The Journal of Physical Chemistry Letters* **1**, 2334-2338 (2010).

64 Murphy, J. E., Beard, M. C., Norman, A. G., Ahrenkiel, S. P., Johnson, J. C., Yu, P., Mićić, O. I., Ellingson, R. J. & Nozik, A. J. PbTe Colloidal Nanocrystals: Synthesis, Characterization, and Multiple Exciton Generation. *Journal of the American Chemical Society* **128**, 3241-3247 (2006).

65 Protesescu, L., Zünd, T., Bodnarchuk, M. I. & Kovalenko, M. V. Air-Stable, Near- to Mid-Infrared Emitting Solids of PbTe/CdTe Core–Shell Colloidal quantum dots. *ChemPhysChem* **17**, 670-674 (2016).

66 Sung, Y., Lee, W., Lee, E., Ko, Y. H. & Kim, S. Ion-Pair Ligand-Assisted Surface Stoichiometry Control of Ag2S Nanocrystals. *Chemistry of Materials* **34**, 9945-9954 (2022).

67 He, H., Lin, Y., Tian, Z.-Q., Zhu, D.-L., Zhang, Z.-L. & Pang, D.-W. Ultrasmall Pb:Ag2S Quantum Dots with Uniform Particle Size and Bright Tunable Fluorescence in the NIR-II Window. *Small* **14**, 1703296 (2018).

68 Zhu, C.-N., Jiang, P., Zhang, Z.-L., Zhu, D.-L., Tian, Z.-Q. & Pang, D.-W. Ag2Se Quantum Dots with Tunable Emission in the Second Near-Infrared Window. *ACS Applied Materials & Interfaces* **5**, 1186-1189 (2013).

69 Ding, Q., Zhao, J., Zhang, H., Li, C., Sun, M., Chen, C., Lin, H., Xu, C., Kuang, H. & Xu, L. Enantiomeric NIR-II Emitting Rare-Earth-Doped Ag2Se Nanoparticles with Differentiated In Vivo Imaging Efficiencies. *Angewandte Chemie* **134**, e202210370 (2022).

70 Wheeler, L. M., Anderson, N. C., Palomaki, P. K. B., Blackburn, J. L., Johnson, J. C. & Neale, N. R. Silyl Radical Abstraction in the Functionalization of Plasma-Synthesized Silicon Nanocrystals. *Chemistry of Materials* **27**, 6869-6878 (2015).

71 Cassette, E., Pons, T., Bouet, C., Helle, M., Bezdetnaya, L., Marchal, F. & Dubertret, B. Synthesis and Characterization of Near-Infrared Cu−In−Se/ZnS Core/Shell Quantum Dots for In vivo Imaging. *Chemistry of Materials* **22**, 6117-6124 (2010).

72 Li, Y., Zhang, P., Tang, W., McHugh, K. J., Kershaw, S. V., Jiao, M., Huang, X., Kalytchuk, S., Perkinson, C. F., Yue, S., Qiao, Y., Zhu, L., Jing, L., Gao, M. & Han, B. Bright, Magnetic NIR-

https://doi.org/10.26434/chemrxiv-2024-jx761 **ORCID:** https://orcid.org/0000-0002-0238-4816 Content not peer-reviewed by ChemRxiv. **License:** CC BY-NC-ND 4.0

II Quantum Dot Probe for Sensitive Dual-Modality Imaging and Intensive Combination Therapy of Cancer. *ACS Nano* **16**, 8076-8094 (2022).

73 Mews, A., Eychmueller, A., Giersig, M., Schooss, D. & Weller, H. Preparation, characterization, and photophysics of the quantum dot quantum well system cadmium sulfide/mercury sulfide/cadmium sulfide. *The Journal of Physical Chemistry* **98**, 934-941 (1994).

74 Kovalenko, M. V., Kaufmann, E., Pachinger, D., Roither, J., Huber, M., Stangl, J., Hesser, G., Schäffler, F. & Heiss, W. Colloidal HgTe Nanocrystals with Widely Tunable Narrow Band Gap Energies: From Telecommunications to Molecular Vibrations. *Journal of the American Chemical Society* **128**, 3516-3517 (2006).

75 Kershaw, S. V., Yiu, W. K., Sergeev, A. & Rogach, A. L. Development of Synthetic Methods to Grow Long-Wavelength Infrared-Emitting HgTe Quantum Dots in Dimethylformamide. *Chemistry of Materials* **32**, 3930-3943 (2020).

76 Cho, W., Kim, S., Coropceanu, I., Srivastava, V., Diroll, B. T., Hazarika, A., Fedin, I., Galli, G., Schaller, R. D. & Talapin, D. V. Direct Synthesis of Six-Monolayer (1.9 nm) Thick Zinc-Blende CdSe Nanoplatelets Emitting at 585 nm. *Chemistry of Materials* **30**, 6957-6960 (2018).

77 Haus, J. W., Zhou, H. S., Honma, I. & Komiyama, H. Quantum confinement in semiconductor heterostructure nanometer-size particles. *Physical Review B* **47**, 1359-1365 (1993).

https://doi.org/10.26434/chemrxiv-2024-jx761 **ORCID:** https://orcid.org/0000-0002-0238-4816 Content not peer-reviewed by ChemRxiv. **License:** CC BY-NC-ND 4.0